FOUNDATIONS OF CIVIL AND ENVIRONMENTAL ENGINEERING

No. 7 2006

Wojciech DORNOWSKI, Piotr PERZYNA[*1]
[1]Institute of Fundamental Technological Research, Polish Academy of Sciences
Świętokrzyska 21, 00–049 Warsaw, Poland

NUMERICAL INVESTIGATION OF LOCALIZED FRACTURE PHENOMENA IN INELASTIC SOLIDS

Received: 12 July 2006
Accepted: 27 August 2006

The main objective of the present paper is to discuss a very efficient procedure of the numerical investigation of localized fracture in inelastic solids generated by impact–loaded adiabatic processes. Particular attention is focused on the proper description of a ductile mode of fracture propagating along the shear band for high impact velocities. This procedure of investigation is based on the utilization of the finite difference method for regularized thermo–elasto–viscoplastic constitutive model of damaged material.

A general constitutive model of thermo–elasto–viscoplastic damaged polycrystalline solids with a finite set of internal variables is used. The set of internal state variables consists of two scalars, namely equivalent inelastic deformation and volume fraction porosity. The equivalent inelastic deformation can describe the dissipation effects generated by viscoplastic flow phenomena and the volume fraction porosity takes into account the microdamage evolution effects. The relaxation time is used as a regularization parameter. Fracture criterion based on the evolution of microdamage is assumed.

As a numerical example we consider dynamic shear band propagation and localized fracture in an asymmetrically impact–loaded prenotched thin plate. The impact loading is simulated by a velocity boundary condition which are the results of dynamic contact problem. The separation of the projectile from the specimen, resulting from wave reflections within the projectile and the specimen, occurs in the phenomenon.

A thin shear band region of finite width which undergoes significant deformation and temperature rise has been determined. Its evolution until occurrence of final fracture has been simulated. Shear band advance as a function of time, the evolution of the Mises stress, equivalent plastic deformation, temperature, the microdamage and the crack path in the fracture region have been determined. Qualitative comparison of numerical results with experimental observation data has been presented. The numerical results obtained

[*] Corresponding author. Tel.: +48 22 8261281 ext.210; fax: +48 22 8269815.
E-mail address: pperzyna@ippt.gov.pl (P. Perzyna)

ISSN 1642-9303

have proven the usefulness of the thermo–elasto–viscoplastic theory in the investigation of dynamic shear band propagations and localized fracture.

1. PROLOGUE

In technological processes fracture can occur as a result of an adiabatic shear band localization generally attributed to a plastic instability generated by intrinsic microdamage mechanisms within a material and thermal softening during plastic deformation.

Recent experimental observations have shown that the shear band procreates in a region of a body deformed where the resistance to plastic deformation is lower and the predisposition for localized shear band formation is higher. In the explanation of the fracture phenomenon along shear band regions very important role has the microdamage process which consists of the nucleation, growth and coalescence of microcracks. It has been found experimentally that in dynamic processes the shear band regions behave differently than adjacent zones. Within the shear band region the deformation process is characterized by very large strains (shear band strains over 100%) and very high strain rates ($10^4 - 10^6$ s^{-1}). The strain rate sensitivity of a material becomes very important feature of the shear band region and the microdamage process is intensified. The mechanism of final failure is a simple propagation of a macrocrack along the damaged material within the shear band region.

The main objective of the present paper is to discuss a very efficient procedure of the numerical investigation of localized fracture in inelastic solids generated by impact–loaded adiabatic processes. Particular attention is focused on the proper description of a ductile mode of fracture propagating along the shear band for high impact velocities.

This procedure of investigation is based on utilization of the finite difference for regularized thermo–elasto–viscoplastic constitutive model of damaged material.

A general constitutive model of thermo–elasto–viscoplastic damaged polycrystalline solids with a finite set of internal state variables is used. The set of internal state variables consists of two scalars, namely equivalent inelastic deformation and volume fraction porosity. The equivalent inelastic deformation can describe the dissipation effects generated by viscoplastic flow phenomena and the volume fraction porosity takes into account the microdamage evolution effects. The relaxation time is used as a regularization parameter. Fracture criterion based on the evolution of microdamage is assumed.

The identification procedure for the material functions and constants involved in the constitutive equations is developed basing on the experimental observations of adiabatic shear bands in an AISI 4340 steel presented by Chak-

rabarti and Spretnak (1975), cf. also Cho, Chi and Duffy (1988) and Chi et al. (1988).

As a numerical example let us consider dynamic shear band propagation and localized fracture in an asymmetrically impact–loaded prenotched thin plate. The plate is made of an AISI 4340 steel. A notch (50 mm wide) is situated symmetrically on the edge. The constant velocity $V_0 = 20$ m/s is imposed for projectile. The projectile comes into contact with the specimen over the width of 50 mm.

The impact loading is simulated by velocity boundary conditions which are the results of dynamic contact problem. The velocity imposed in specimen in front of projectile increases during the process. The separation of the projectile from the specimen, resulting from wave reflections within the projectile and the specimen, occurs in the phenomenon. All surface areas have traction free boundary conditions except where the velocity boundary condition is applied. We idealize the initial boundary value problem observed experimentally in Guduru, Rosakis and Ravichandran (2001), by assuming the velocity boundary condition and different material of the specimen. The discretization parameters are assumed in such a way, that allows to solve the problem of mesomechanics properly. The dimension of the accepted mesh is of order 40 μm. A thin shear band region of finite width which undergoes significant deformation and temperature rise has been determined. Its evolution until occurrence of final fracture has been simulated. Shear band advance as a function of time, and the evolution of the Mises stress, equivalent plastic deformation, temperature, the microdamage and the crack path in the fracture region have been determined. Qualitative comparison of numerical results with experimental observation data has been presented. The numerical results obtained have proven the usefulness of the thermo–elasto–viscoplastic theory in the numerical investigation of dynamic shear band propagation and localized fracture.

2. PHYSICAL AND EXPERIMENTAL MOTIVATION

2.1. Analysis of mesomechanical problems

In modern technology we recently observe a very important application of metals, ceramics and polymers at mesoscale. Micromachines within this size range clearly will be of increasing technological significance. Processes that control the mechanical integrity of microelectronic devices take also place on this size scale, cf. Needlemen (2000) and Hutchinson (2000).

There is considerable experimental evidence that plastic flow and particularly localization of plastic deformation and fracture phenomena in crystalline solids are inherently size dependent over mesoscale range. It is generally ac-

cepted that: "smaller is stronger" or "smaller is harder".

Plastic behaviour at mesoscale range can not be characterized by conventional plasticity theories because they incorporate no material length scale and predict no size effect.

In recent years a variety of theoretical frameworks are emerging to describe inelastic deformation at the mesoscale. Four such frameworks (constitutive structures), each involving a length scale, are as follows: (i) discrete dislocation plasticity; (ii) nonlocal plasticity; (iii) the coupling of matter diffusion and deformation; (iv) elasto–viscoplasticity.

The mesomechanical problems also pose numerical challenges. Computations on smaller size scale require smaller time steps. Since size dependent phenomena come into play when there are gradients of deformation and stress, hence numerical methods are usually needed to obtain solutions. Finite strains and rotations have to be taken into consideration.

While approaching the mesoscale problems the dominant numerical methods are the finite element and finite difference methods.

It is noteworthy to add that the mesoscale continuum mechanics is in an early stage of development, both in terms of the theoretical framework as well as the computational methods.

In our considerations we shall use the thermo–elasto–viscoplasticity as a constitutive model of the material and apply the finite difference method in numerical computations.

2.2. Experimental investigation of the initiation and propagation of shear bands

Guduru, Rosakis and Ravichandran (2001) presented an experimental investigation of the initiation and propagation characteristics of dynamic shear band in C300 maraging steel. An elastic discharge machining (EDM) notch (260 μm wide) was further extended by 2 mm by fatigue loading, cf. Fig. 1.

In experimental investigation of Guduru, Rosakis and Ravichandran (2001), two diagnostic techniques were used to observe the crack tip, the propagating shear band and the temperature field evolution during the initiation and propagation of the shear band. On one side of the specimen, the optical technique of coherent gradient sensing (CGS) in reflection was used to monitor the evolution of the stress intensity factors as a function of time. On the other side of specimen, a newly developed full–field, high–speed infrared (IR) imaging system was employed to measure the evolution of 2–D temperature field, cf. Fig. 2. They measure the advance of the shear band and its velocity in five different experiments, cf. Fig. 3 and 4. The shear band velocity can be seen to be highly transient and to be a function of the impact speed. In all but one experiment, the band arrests momentarily at about 30 μs, before accelerating to high speeds. The maximum shear band velocity observed here is about 1100 m/s, cf. also

Zhou et al. (1996).

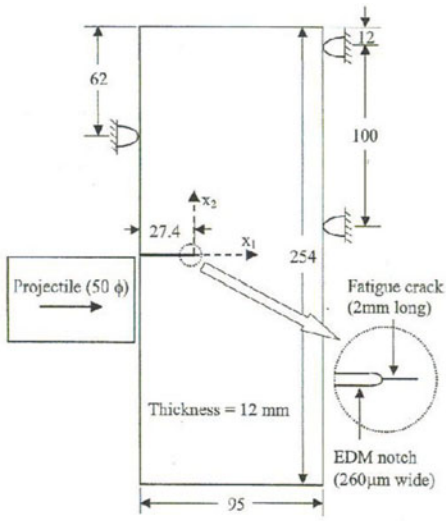

Fig. 1. Specimen geometry and impact arrangement. The projectile is 127 mm long. All dimensions shown are in millimetres. (After Guduru, Rosakis and Ravichandran (2001))

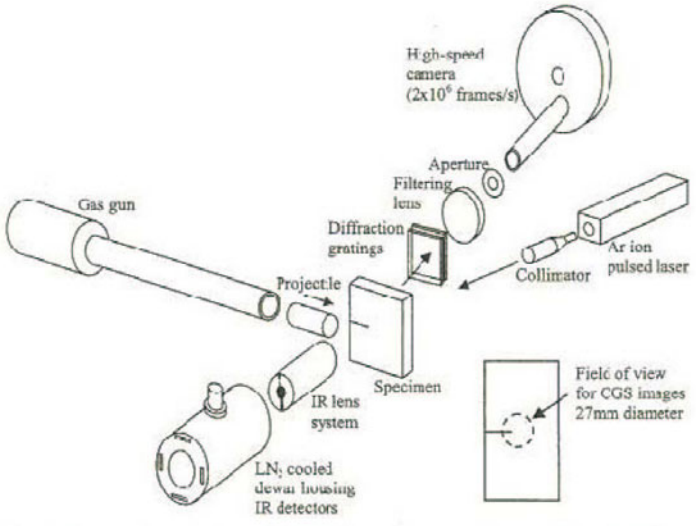

Fig. 2. Schematic illustration of the experimental setup. The CGS setup measures the out plane displacement gradients on the rear side of the specimen. Simultaneous thermal imaging is accomplished using the IR camera on the facing side of the specimen. (After Guduru, Rosakis and Ravichandran (2001)).

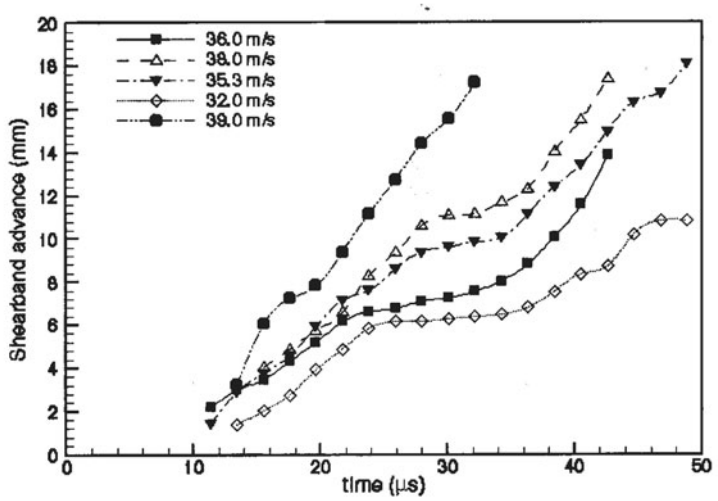

Fig. 3. Shear band advance as a function of time. (After Guduru, Rosakis and Ravichandran (2001)).

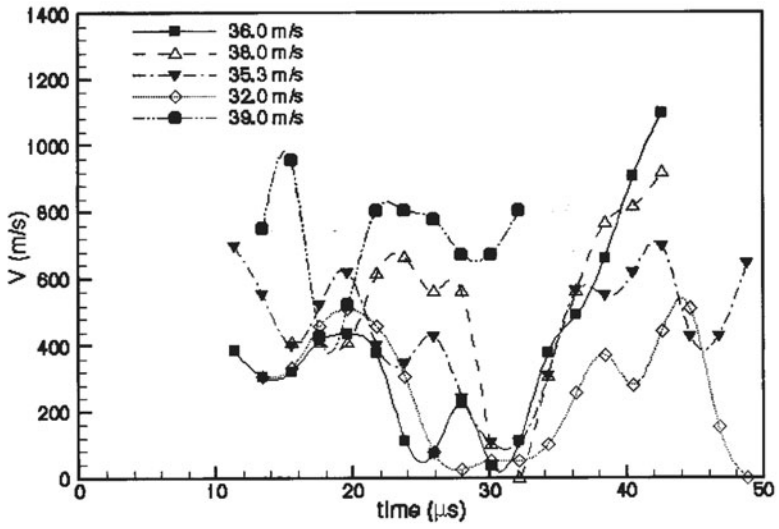

Fig. 4. Shear band velocity as a function of time. (After Guduru, Rosakis and Ravichandran (2001)).

2.3. Fracture phenomena along localized shear bands

Fractured specimens were examined using an optical microscope to study the features of the shear bands such as its width, trajectory, the fracture surface, etc. The shear band is revealed as a white stripe. The thickness of the band is about 40 μm, cf. Fig. 5. A scanning electron microscope (SEM) image of the specimen surface, which failed by shear band propagation, shows elongated voids, with sheared edges that are characteristic of such a failure mode, cf. Fig. 6. The presence of voids reveals the development of triaxiality tensile stress state that led to void growth and eventual fracture.

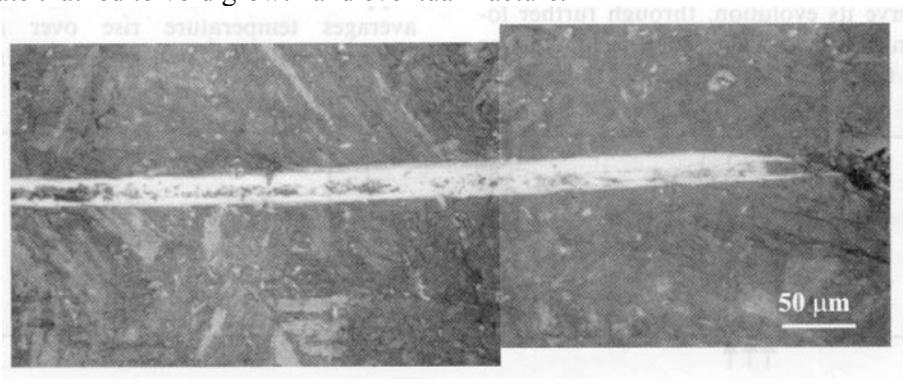

Fig. 5. An optical micrograph of an arrested shear band. (After Guduru, Rosakis and Ravichandran (2001)).

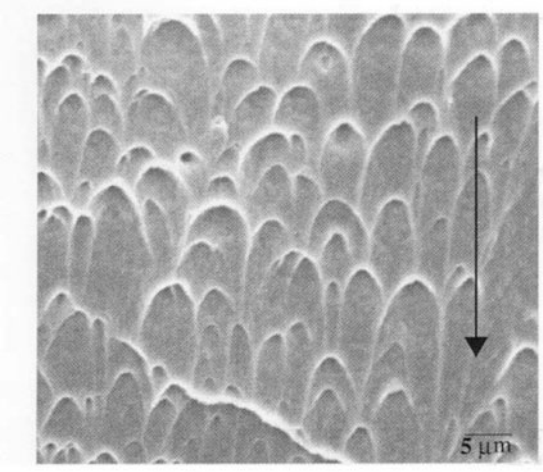

Fig. 6. An SEM image of the fracture surface that failed by shear banding. Arrow shows the crack propagation direction. (After Guduru, Rosakis and Ravichandran (2001)).

2.4. Temperature measurement

Guduru, Rosakis and Ravichandran (2001) also performed broad experimental observations of the temperature field evolution during the initiation and propagation of the shear band. One of their objectives of imaging the temperature field was to visualize the development of the plastic zone at the tip of the initial crack and to observe its evolution, through further localization, into a shear band. The IR camera was focused at the tip of the fatigue crack as illustrated on the left–hand side of Fig. 7 The impact speed was 35 m/s. They show a sequence of thermal images revealing the development of the temperature field as a function of time. Starting at about 21 μ s, the central hot region extends to the right, as indicated by the contour lines, signifying the process of shear localization. The measured highest temperature rise within the plastic zone when this happened was at least 80 K, cf. Fig. 7.

Let us now focus our attention on the temperature field associated with the tip of a propagating shear band. The gradual nature of temperature rise at the front end of shear band supports the notion of a very diffuse shear band tip, as opposed to a crack tip which carries a strong singularity in the field quantities.

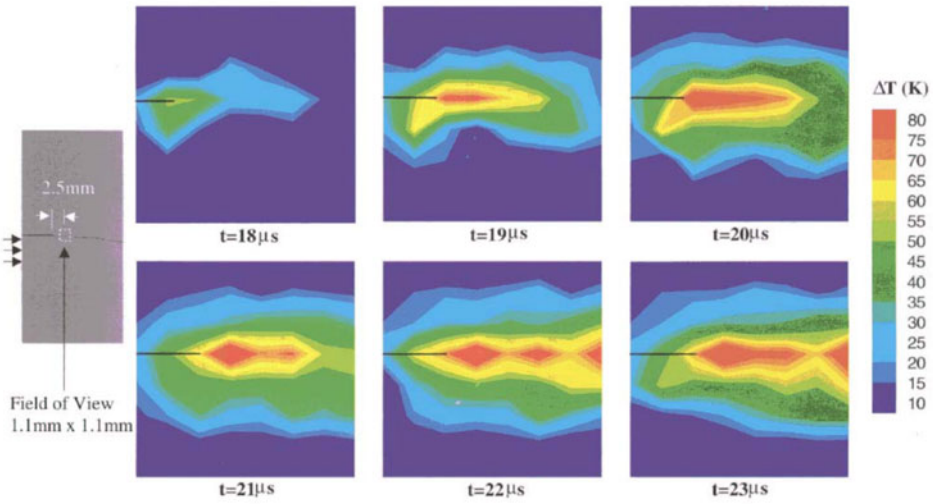

Fig. 7. A sequence of thermal images showing the transition of crack tip plastic zone in to a shear band. (After Guduru, Rosakis and Ravichandran (2001)).

As the shear band propagates, the material within the band progressively accumulates large plastic shear strains within short times and the temperature can quickly reach a very high value. The temperature distribution along a well–defined shear band has been of special interest in the investigation of Guduru, Rosakis and Ravichandran (2001). They have been consistently observed, in all

experiments where a propagating shear band was imaged, that the temperature distribution along the band is highly non–uniform, with discrete regions of high temperature, that look like "hot spots". These hot spots are also seen to translate along the length of the band.

2.5. Possible shear band branching

Guduru, Rosakis and Ravichandran (2001) also discussed the possibility of shear band branching. Figure 8 shows their three micrographs that confirm previous observation about the possibility of shear band branching mode by Meyers (1994). In the first two, the left edges are the failure paths, caused by a propagating shear band. The third image is taken from an arrested shear band. The branching behaviour is clearly seen in all three cases. They added that currently there is no theoretical framework to explain such a phenomenon and they stressed that this interesting observation requires further investigation to understand the conditions under which such a bifurcation can take place.

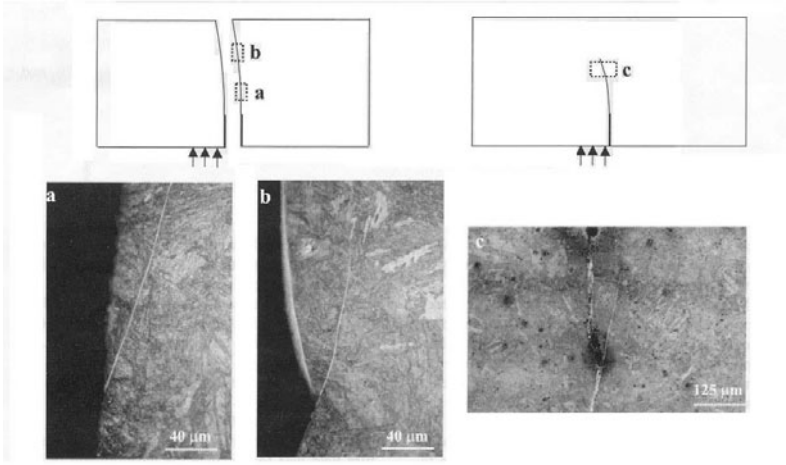

Fig. 8. Optical micrographs of possible shear band bifurcation. (After Guduru, Rosakis and Ravichandran (2001)).

3. THERMO–ELASTO–VISCOPLASTIC MODEL OF A MATERIAL

3.1. Basic assumptions and definitions

Let us assume that a continuum body is an open bounded set $B \subset IR^3$, and let $\phi : B \to S$ be a C^1 configuration of B in S. The tangent of ϕ is denoted $\mathbf{F} = T\phi$ and is called the deformation gradient of ϕ.

Let $\{X^A\}$ and $\{x^a\}$ denote coordinate systems on B and S respectively. Then we refer to $B \subset IR^3$ as the reference configuration of a continuum body with particles $X \in B$ and to $S = \phi(B)$ as the current configuration with points $\mathbf{x} \in S$. The matrix $\mathbf{F}(\mathbf{X},t) = \partial\phi(\mathbf{X},t)/\partial\mathbf{X}$ with respect to the coordinate bases $\mathbf{E}_A(\mathbf{X})$ and $\mathbf{e}_a(\mathbf{x})$ is given by

$$F_A^a(\mathbf{X},t) = \frac{\partial \phi^a}{\partial X^A}(\mathbf{X},t), \tag{1}$$

where a mapping $\mathbf{x} = \phi(\mathbf{X},t)$ represents a motion of a body B.

We consider the local multiplicative decomposition

$$\mathbf{F} = \mathbf{F}^e \cdot \mathbf{F}^p, \tag{2}$$

where $(\mathbf{F}^e)^{-1}$ is the deformation gradient that releases elastically the stress on the neighbourhood $\phi(N(\mathbf{X}))$ in the current configuration.

Let us define the total and elastic Finger deformation tensors

$$\mathbf{b} = \mathbf{F} \cdot \mathbf{F}^T, \quad \mathbf{b}^e = \mathbf{F}^e \cdot \mathbf{F}^{e^T}, \tag{3}$$

respectively, and the Eulerian strain tensors as follows

$$\mathbf{e} = \frac{1}{2}(\mathbf{g} - \mathbf{b}^{-1}), \quad \mathbf{e}^e = \frac{1}{2}(\mathbf{g} - \mathbf{b}^{e^{-1}}), \tag{4}$$

where $\mathbf{g}$ denotes the metric tensor in the current configuration.

By definition[1]

$$\mathbf{e}^p = \mathbf{e} - \mathbf{e}^e = \frac{1}{2}(\mathbf{b}^{e^{-1}} - \mathbf{b}^{-1}) \tag{5}$$

we introduce the plastic Eulerian strain tensor.

To define objective rates for vectors and tensors we use the Lie derivative[2]. Let us define the Lie derivative of a spatial tensor field $\mathbf{t}$ with respect to the velocity field υ as

$$\mathrm{L}_{\upsilon}\mathbf{t} = \phi_* \frac{\partial}{\partial t}(\phi^* \mathbf{t}), \tag{6}$$

[1]For precise definition of the finite elasto–plastic deformation see Perzyna (1995).

[2]The algebraic and dynamic interpretations of the Lie derivative have been presented by Abraham et al. (1988), cf. also Marsden and Hughes (1983).

where ϕ^* and ϕ_* denote the pull–back and push–forward operations, respectively.

The rate of deformation tensor is defined as follows

$$\mathbf{d}^\flat = \mathrm{L}_{\upsilon}\mathbf{e}^\flat = \frac{1}{2}\mathrm{L}_{\upsilon}\mathbf{g} = \frac{1}{2}\left(g_{ac}\upsilon^c\,|_b + g_{cb}\upsilon^c\,|_a\right)\mathbf{e}^a \otimes \mathbf{e}^b, \tag{7}$$

where the symbol $\flat$ denotes the index lowering operator and $\otimes$ the tensor product,

$$\upsilon^a\,|_b = \frac{\partial \upsilon^a}{\partial x^b} + \gamma^a_{bc}\upsilon^c, \tag{8}$$

and γ^a_{bc} denotes the Christoffel symbol for the general coordinate systems $\{x^a\}$. The components of the spin ω are given by

$$\omega_{ab} = \frac{1}{2}\left(g_{ac}\upsilon^c\,|_b - g_{cb}\upsilon^c\,|_a\right) = \frac{1}{2}\left(\frac{\partial \upsilon_a}{\partial x^b} - \frac{\partial \upsilon_b}{\partial x^a}\right). \tag{9}$$

Similarly

$$\mathbf{d}^{e^\flat} = \mathrm{L}_{\upsilon}\mathbf{e}^{e^\flat}, \quad \mathbf{d}^{p^\flat} = \mathrm{L}_{\upsilon}\mathbf{e}^{p^\flat}, \tag{10}$$

and

$$\mathbf{d} = \mathbf{d}^e + \mathbf{d}^p. \tag{11}$$

Let τ denote the Kirchhoff stress tensor related to the Cauchy stress tensor σ by

$$\tau = J\sigma = \frac{\rho_{Ref}}{\rho}\sigma, \tag{12}$$

where the Jacobian J is the determinant of the linear transformation $\mathbf{F}(\mathbf{X},t) = (\partial/\partial X)\phi(\mathbf{X},t)$, $\rho_{Ref}(\mathbf{X})$ and $\rho(\mathbf{x},t)$ denote the mass density in the reference and current configuration, respectively.

The Lie derivative of the Kirchhoff stress tensor $\tau \in \mathbf{T}^2(S)$ (elements of $\mathbf{T}^2(S)$ are called tensors on S, contravariant of order 2) gives

$$\mathrm{L}_{\upsilon}\tau = \phi_* \frac{\partial}{\partial t}(\phi^*\tau)$$

$$= \left\{ \mathbf{F} \cdot \frac{\partial}{\partial t} [\mathbf{F}^{-1} \cdot (\tau \circ \phi) \cdot \mathbf{F}^{-1^T}] \cdot \mathbf{F}^T \right\} \circ \phi^{-1}$$
$$= \dot{\tau} - (\mathbf{d} + \omega) \cdot \tau - \tau \cdot (\mathbf{d} + \omega)^T, \tag{13}$$

where $\circ$ denotes the composition of mappings. In the coordinate system (13) reads

$$(\mathrm{L}_{\upsilon} \tau)^{ab} = F^a_A \frac{\partial}{\partial t} (F^{-1\,A}_c \tau^{cd} F^{-1\,B}_d) F^b_B \tag{14}$$
$$= \frac{\partial \tau^{ab}}{\partial t} + \frac{\partial \tau^{ab}}{\partial x^c} \upsilon^c - \tau^{cb} \frac{\partial \upsilon^a}{\partial x^c} - \tau^{ac} \frac{\partial \upsilon^b}{\partial x^c}.$$

Equation (14) defines the Oldroyd rate of the Kirchhoff stress tensor τ (cf. Oldroyd (1950)).

3.2. Constitutive postulates

Let us assume that: (i) conservation of mass, (ii) balance of momentum, (iii) balance of moment of momentum, (iv) balance of energy, (v) entropy production inequality hold.

We introduce the four fundamental postulates:

i) Existence of the free energy function. It is assumed that the free energy function is given by

$$\psi = \hat{\psi}(\mathbf{e}, \mathbf{F}, \vartheta; \boldsymbol{\mu}), \tag{15}$$

where $\mathbf{e}$ denotes the Eulerian strain tensor, $\mathbf{F}$ is deformation gradient, ϑ temperature and $\boldsymbol{\mu}$ denotes a set of the internal state variables. To extend the domain of the description of the material properties and particularly to take into consideration different dissipation effects we have to introduce the internal state variables represented by the vector $\boldsymbol{\mu}$.

ii) Axiom of objectivity (spatial covariance). The constitutive structure should be invariant with respect to any diffeomorphism (any motion) $\xi : S \to S$ (cf. Marsden and Hughes (1983)). Assuming that $\xi : S \to S$ is a regular, orientation preserving map transforming $\mathbf{x}$ into $\mathbf{x}'$ and $T\xi$ is an isometry from $T_{\mathbf{x}}S$ to $T_{\mathbf{x}'}S$, we obtain the axiom of material frame indifference (cf. Truesdell and Noll (1965)).

iii) The axiom of the entropy production. For any regular motion of a body

B the constitutive functions are assumed to satisfy the reduced dissipation inequality

$$\frac{1}{\rho_{Ref}}\tau : \mathbf{d} - (\eta\dot{\vartheta} + \dot{\psi}) - \frac{1}{\rho\vartheta}\mathbf{q}\cdot\operatorname{grad}\vartheta \geq 0, \tag{16}$$

where ρ_{Ref} and ρ denote the mass density in the reference and actual-configuration, respectively, τ is the Kirchhoff stress tensor, $\mathbf{d}$ the rate of deformation, η is the specific (per unit mass) entropy, and $\mathbf{q}$ denotes the heat flow vector field. Marsden and Hughes (1983) proved that the reduced dissipation inequality (16) is equivalent to the entropy production inequality first introduced by Coleman and Noll (1963) in the form of the Clausius–Duhem inequality. In fact the Clausius–Duhem inequality gives a statement of the second law of thermodynamics within the framework of mechanics of continuous media, cf. Duszek and Perzyna (1991).

iv) The evolution equation for the internal state variable vector $\boldsymbol{\mu}$ is assumed in the form as follows

$$\mathrm{L}_{\upsilon}\mu = \hat{\mathbf{m}}(\mathbf{e}, \mathbf{F}, \vartheta, \mu), \tag{17}$$

where the evolution function $\hat{\mathbf{m}}$ has to be determined based on careful physical interpretation of a set of internal state variables and analysis of available experimental observations. The determination of the evolution function $\hat{\mathbf{m}}$ (in practice a finite set of the evolution functions) appears to be the main problem of the modern constitutive modelling.

The main objective is to develop the rate type constitutive structure for an elastic–viscoplastic material in which the effects of the plastic non–normality, micro–damaged mechanism and thermomechanical coupling are taken into consideration. To do this it is sufficient to assume a finite set of the internal state variables. For our practical purposes it is sufficient to assume that the internal state vector $\boldsymbol{\mu}$ has the form

$$\boldsymbol{\mu} = (\in^{p}, \xi), \tag{18}$$

where $\in^{p}$ is the equivalent viscoplastic deformation, i.e.

$$\in^{p} = \int_0^t \left(\frac{2}{3}\mathbf{d}^{p} : \mathbf{d}^{p}\right)^{\frac{1}{2}} \mathrm{d}t, \tag{19}$$

and ξ is volume fraction porosity and takes account for micro–damaged effects.

Let us introduce the plastic potential function $f = f(J_1, J_2, \vartheta, \boldsymbol{\mu})$, where J_1, J_2 denote the first two invariants of the Kirchhoff stress tensor τ.

Let us postulate the evolution equations as follows

$$\mathbf{d}^p = \Lambda \mathbf{P}, \qquad \dot{\xi} = \Xi, \tag{20}$$

where for elasto–viscoplastic model of a material we assume (cf. Perzyna (1963, 1966, 1971, 1995))

$$\Lambda = \frac{1}{T_m} \left\langle \Phi\left(\frac{f}{\kappa} - 1\right) \right\rangle, \tag{21}$$

T_m denotes the relaxation time for mechanical disturbances, the isotropic work–hardening–softening function κ is

$$\kappa = \hat{\kappa}(\in^p, \vartheta, \xi), \tag{22}$$

Φ is the empirical overstress function, the bracket $\langle . \rangle$ defines the ramp function,

$$\mathbf{P} = \left.\frac{\partial f}{\partial \tau}\right|_{\xi = const} \left(\left\| \frac{\partial f}{\partial \tau} \right\| \right)^{-1}, \tag{23}$$

Ξ denotes the evolution function which has to be determined.

3.3. Intrinsic micro–damage mechanisms

To take into consideration the experimentally observed time dependent effects it is advantageous to use the proposition of the description of the intrinsic micro–damage process presented by Perzyna (1986a,b) and Duszek–Perzyna and Perzyna (1994).

Let us assume that the intrinsic micro–damage process consists of the nucleation and growth mechanisms[3].

Physical considerations (cf. Curran et al. (1987) and Perzyna (1986a,b)) have shown that the nucleation of microvoids in dynamic loading processes which are characterized by very short time duration is governed by the thermally–activated mechanism. Based on this heuristic suggestion and taking into

[3]Recent experimental observation results (cf. Shockey et al. (1985)) have shown that coalescence mechanism can be treated as nucleation and growth process on a smaller scale. This conjecture simplifies very much the description of the intrinsic micro–damage process by taking account only of the nucleation and growth mechanisms.

account the influence of the stress triaxiality on the nucleation mechanism we postulate for rate dependent plastic flow[4]

$$\left(\dot{\xi}\right)_{nucl} = \frac{1}{T_m} h^*(\xi,\vartheta)\left[\exp\frac{m^*(\vartheta)\,|\,I_n - \tau_n(\xi,\vartheta,\in^p)\,|}{k\vartheta} - 1\right], \tag{24}$$

where k denotes the Boltzmann constant, $h^*(\xi,\vartheta)$ represents a void nucleation material function which is introduced to take account of the effect of microvoid interaction, $m^*(\vartheta)$ is a temperature dependent coefficient, $\tau_n(\xi,\vartheta,\in^p)$ is the porosity, temperature and equivalent plastic strain dependent threshold stress for microvoid nucleation,

$$I_n = a_1 J_1 + a_2\sqrt{J_2^{'}} + a_3\left(J_3^{'}\right)^{\frac{1}{3}} \tag{25}$$

defines the stress intensity invariant for nucleation, a_i $(i=1,2,3)$ are the material constants, J_1 denotes the first invariant of the Kirchhoff stress tensor τ, $J_2^{'}$ and $J_3^{'}$ are the second and third invariants of the stress deviator $\tau^{'}$.

For the growth mechanism we postulate (cf. Johnson (1981); Perzyna (1986a,b); Perzyna and Drabik (1989, 2005) and Dornowski and Perzyna (1999, 2000, 2002))

$$\left(\dot{\xi}\right)_{grow} = \frac{1}{T_m}\frac{g^*(\xi,\vartheta)}{\kappa_0}\left[I_g - \tau_{eq}(\xi,\vartheta,\in^p)\right], \tag{26}$$

where $T_m\kappa_0$ denotes the dynamic viscosity of a material, $g^*(\xi,\vartheta)$ represents a void growth material function and takes account for void interaction, $\tau_{eq}(\xi,\vartheta,\in^p)$ is the porosity, temperature and equivalent plastic strain dependent void growth threshold stress,

$$I_g = b_1 J_1 + b_2\sqrt{J_2^{'}} + b_3\left(J_3^{'}\right)^{\frac{1}{3}}, \tag{27}$$

defines the stress intensity invariant for growth and b_i $(i=1,2,3)$ are the material constants.

[4]An analysis of the experimental observations for cycle fatigue damage mechanics at high temperature of metals performed by Sidey and Coffin (1979) suggests that the intrinsic micro–damage process does very much depend on the strain rate effects, the wave shape effects as well as on the stress tiaxiality.

Finally the evolution equation for the porosity ξ has the form

$$\dot{\xi} = \frac{h^*(\xi,\vartheta)}{T_m}\left[\exp\frac{m^*(\vartheta)\,|\,I_n - \tau_n(\xi,\vartheta,\in^p)\,|}{k\vartheta} - 1\right] + \frac{g^*(\xi,\vartheta)}{T_m\kappa_0}\Big[I_g - \tau_{eq}(\xi,\vartheta,\in^p)\Big]. \tag{28}$$

To have consistent theory of elasto–viscoplasticity we can replace the exponential function in the nucleation term and the linear function in the growth term by the empirical overstress Φ, then the evolution equation for the porosity ξ takes the form as follows (cf. Perzyna (2005))

$$\dot{\xi} = \frac{1}{T_m}h^*(\xi,\vartheta)\left\langle \Phi[\frac{I_n}{\tau_n(\xi,\vartheta,\in^p)} - 1]\right\rangle + \frac{1}{T_m}g^*(\xi,\vartheta)\left\langle \Phi[\frac{I_g}{\tau_n(\xi,\vartheta,\in^p)} - 1]\right\rangle. \tag{29}$$

This determines the evolution function Ξ.

3.4. Thermodynamic restrictions and rate type constitutive equations

Suppose the axiom of the entropy production holds. Then the constitutive assumption (15) and the evolution equations (20) lead to the results as follows

$$\tau = \rho_{Ref}\frac{\partial\hat{\psi}}{\partial\mathbf{e}}, \quad \eta = -\frac{\partial\hat{\psi}}{\partial\vartheta}, \quad -\frac{\partial\hat{\psi}}{\partial\mu}\cdot \mathrm{L}_{\upsilon}\mu - \frac{1}{\rho\vartheta}\mathbf{q}\cdot\operatorname{grad}\vartheta \geq 0. \tag{30}$$

The rate of internal dissipation is determined by

$$\vartheta\hat{i} = -\frac{\partial\hat{\psi}}{\partial\mu}\cdot \mathrm{L}_{\upsilon}\mu = -\left(\frac{\partial\hat{\psi}}{\partial\in^p}\sqrt{\frac{2}{3}}\right)\Lambda - \frac{\partial\hat{\psi}}{\partial\xi}\Xi. \tag{31}$$

Operating on the stress relation $(30)_1$ with the Lie derivative and keeping the internal state vector constant, we obtain (cf. Duszek–Perzyna and Perzyna (1994))

$$\mathrm{L}_{\upsilon}\tau = L^e : \mathbf{d} - L^{th}\dot{\vartheta} - \Big[(L^e + \mathbf{g}\tau + \tau\mathbf{g}) : \mathbf{P}\Big]\frac{1}{T_m}\left\langle \Phi(\frac{f}{\kappa} - 1)\right\rangle, \tag{32}$$

where

$$L^e = \rho_{Ref}\frac{\partial^2\hat{\psi}}{\partial \mathbf{e}^2}, \qquad L^{th} = -\rho_{Ref}\frac{\partial^2\hat{\psi}}{\partial \mathbf{e}\partial\vartheta}. \tag{33}$$

Substituting $\dot{\psi}$ into the energy balance equation and taking into account the results $(30)_3$ and (31) gives

$$\rho\vartheta\dot{\eta} = -\mathrm{div}\mathbf{q} + \rho\vartheta\hat{i}. \tag{34}$$

Operating on the entropy relation $(30)_2$ with the Lie derivative and substituting the result into (34) we obtain

$$\rho c_p\dot{\vartheta} = -\mathrm{div}\mathbf{q} + \vartheta\frac{\rho}{\rho_{Ref}}\frac{\partial\tau}{\partial\vartheta}:\mathbf{d} + \rho\chi^{*}\tau:\mathbf{d}^{p} + \rho\chi^{**}\dot{\xi}, \tag{35}$$

where the specific heat

$$c_p = -\vartheta\frac{\partial^2\hat{\psi}}{\partial\vartheta^2} \tag{36}$$

and the irreversibility coefficients χ^{*} and χ^{**} are determined by

$$\chi^{*} = -\left(\frac{\partial\hat{\psi}}{\partial\in^{p}} - \vartheta\frac{\partial^2\hat{\psi}}{\partial\vartheta\partial\in^{p}}\right)\sqrt{\frac{2}{3}}\frac{1}{\tau:\mathbf{P}}, \tag{37}$$

$$\chi^{**} = -\left(\frac{\partial\hat{\psi}}{\partial\xi} - \vartheta\frac{\partial^2\hat{\psi}}{\partial\vartheta\partial\xi}\right).$$

So, a set of the constitutive equations of the rate type has the form as follows

$$\mathrm{L}_{\upsilon}\tau = L^e:\mathbf{d} - L^{th}\dot{\vartheta} - \left[(L^e + \mathbf{g}\tau + \tau\mathbf{g}):\mathbf{P}\right]\frac{1}{T_m}\left\langle\Phi(\frac{f}{\kappa}-1)\right\rangle,$$

$$\rho c_p\dot{\vartheta} = -\mathrm{div}\mathbf{q} + \vartheta\frac{\rho}{\rho_{Ref}}\frac{\partial\tau}{\partial\vartheta}:\mathbf{d} + \rho\chi^{*}\left\langle\frac{1}{T_m}\Phi(\frac{f}{\kappa}-1)\right\rangle\tau:\mathbf{P} + \rho\chi^{**}\dot{\xi}, \tag{38}$$

$$\dot{\xi} = \frac{1}{T_m}h^{*}(\xi,\vartheta)\left\langle\Phi[\frac{I_n}{\tau_n(\xi,\vartheta,\in^{p})}-1]\right\rangle + \frac{1}{T_m}g^{*}(\xi,\vartheta)\left\langle\Phi[\frac{I_g}{\tau_n(\xi,\vartheta,\in^{p})}-1]\right\rangle.$$

All the material functions and the material constants should be identified based

on available experimental data.

3.5. Fracture criterion based on the evolution of micro–damage

We base the fracture criterion on the evolution of the porosity internal state variable ξ. The volume fraction porosity ξ takes account for microdamage effects.

Let us assume that the catastrophe takes place for $\xi = \xi^F$ (cf. Perzyna (1984)), that is

$$\kappa = \hat{\kappa}(\in^p, \vartheta, \xi)\Big|_{\xi=\xi^F} = 0. \tag{39}$$

It means that for $\xi = \xi^F$ the material loses its carrying capacity. The condition (39) describes the main experimental observation - that the load tends to zero at the fracture point.

It is noteworthy that the isotropic hardening–softening material function $\hat{\kappa}$ proposed in Eq. (22) should satisfy the fracture criterion (39).

3.6. Length–scale sensitivity of the constitutive model

The constitutive equations for a thermo–elastic–viscoplastic model introduce implicitly a length–scale parameter into the dynamic initial–boundary value problem, i.e.

$$l = \alpha c T_m, \tag{40}$$

where T_m is the relaxation time for mechanical disturbances, and is directly related to the viscosity of the material, c denotes the velocity of the propagation of the elastic waves in the problem under consideration, and the proportionality factor α depends on the particular initial–boundary value problem and may also be conditioned on the microscopic properties of the material.

The relaxation time T_m can be viewed either as a microstructural parameter to be determined from experimental observations or as a mathematical regularization parameter.

To go deeply into length–scale sensitivity of the constitutive model let as consider one–dimensional longitudinal wave propagation for an elastic–viscoplastic material. The constitutive equations are assumed in the form as follows

$$\dot{\in}^p = \dot{\in} - \frac{\dot{\sigma}}{E}, \qquad \dot{\sigma} = h\dot{\in}^p + \frac{\sigma_0}{\gamma}\frac{\partial \dot{\in}^p}{\partial t}, \tag{41}$$

where γ denotes the viscosity parameter, σ_0 the yield stress and h the hardening–softening parameter.

The wave equation takes the form

$$\zeta\left(\frac{1}{c^2}\frac{\partial^2 v}{\partial t^2}-\frac{\partial^3 v}{\partial x^2 \partial t}\right)+\frac{E+h}{c^2}\frac{\partial^2 v}{\partial t^2}-h\frac{\partial^2 v}{\partial x^2}=0, \tag{42}$$

where

$$\zeta=\frac{\sigma_0}{\gamma}=\sigma_0 T_m \tag{43}$$

denotes the macroscopic viscosity (or dynamic viscosity) and $c=(E/\rho)^{\frac{1}{2}}$.

For $\gamma\to\infty \Rightarrow \zeta\to 0$ (42) reduces to the wave equation for an elastic–plastic rate independent material. To investigate the dispersive nature of wave propagation in an elastic–viscoplastic medium a general solution for a single linear harmonic wave with angular frequency ω and wave number k is assumed

$$\upsilon=Ae^{i(kx-\omega t)}, \quad k=\frac{2\pi}{\lambda}, \tag{44}$$

and A denotes the amplitude.

To satisfy the equation (42) k and ω have to be related by the dispersion relation

$$\zeta\left(\frac{1}{c^2}\omega^3-k^2\omega\right)i-\frac{E+h}{c^2}\omega^2+hk^2=0. \tag{45}$$

By sophisticated analysis of the dispersion relation (45) we can obtain the result for the internal length–scale parameter (cf. Sluys (1992))

$$l=\frac{2\sigma_0}{E}cT_m. \tag{46}$$

Comparison (46) with (40) gives

$$\alpha=\frac{2\sigma_0}{E} \tag{47}$$

for one–dimensional longitudinal wave propagation problem.

4. FORMULATION OF THE EVOLUTION PROBLEM

4.1. Initial–boundary value problem (evolution problem)

Find φ as function of t and $\mathbf{x}$ satisfying

$$\left.\begin{array}{ll} \text{(i)} & \dot{\varphi} = A(t,\varphi)\varphi + \mathbf{f}(t,\varphi); \\ \text{(ii)} & \varphi(0) = \varphi^0(\mathbf{x}); \\ \text{(iii)} & \text{The boundary conditions;} \end{array}\right\} \tag{48}$$

where the unknown φ takes values in a Banach space, $A(t,\varphi)$ is a spatial linear differential operator (in general unbounded) depending on t and φ, $\mathbf{f}$ is a nonlinear function, and the dot denotes the material derivative.

The evolution problem (48) describes an adiabatic inelastic flow process provided

$$\varphi = [\upsilon \ \rho \ \tau \ \xi \ \ \vartheta]^T, \tag{49}$$

$$\mathbf{f} = \begin{bmatrix} 0 \\ 0 \\ -\dfrac{\left\langle \Phi(\frac{f}{\kappa}-1)\right\rangle}{T_m}\left[\left(L^e + \dfrac{\chi^*\tau}{\rho_{Ref}}L^{th} + \mathbf{g}\tau + \tau\mathbf{g} + W\right):\mathbf{P}\right] - \dfrac{\chi^{**}\Xi}{\rho_{Ref}}L^{th} \\ \Xi \\ \dfrac{1}{T_m}\left\langle \Phi(\dfrac{f}{\kappa}-1)\right\rangle \dfrac{\chi^*}{\rho_{Ref}}L^{th}\tau:\mathbf{P} + \dfrac{\chi^{**}}{\rho_{Ref}}\Xi \end{bmatrix},$$

$$A = \begin{bmatrix} 0 & 0 & \dfrac{\tau}{\rho_{Ref}\rho}\text{grad} & \dfrac{1}{\rho_{Ref}}\text{div} & 0 \\ 0 & -\rho\text{div} & 0 & 0 & 0 \\ 0 & IE:\text{sym}\dfrac{\partial}{\partial\mathbf{x}} + 2\text{sym}(\tau:\dfrac{\partial}{\partial\mathbf{x}}) & 0 & 0 & 0 \\ 0 & 0 & 0 & 0 & 0 \\ 0 & \dfrac{\vartheta}{c_p\rho_{Ref}}\dfrac{\partial\tau}{\partial\vartheta}:\text{sym}\dfrac{\partial}{\partial\mathbf{x}} & 0 & 0 & 0 \end{bmatrix}.$$

where

$$IE = L^e - \frac{\vartheta}{c_p \rho_{Ref}} L^{th} \frac{\partial \tau}{\partial \vartheta} \tag{50}$$

denotes the thermo–elastodynamic matrix for adiabatic process.

4.2. Numerical solution of the evolution problem

The discretization in space and time based on the finite difference method is developed. Rate dependency (viscosity) allows the spatial differential operator in the governing equations to retain its ellipticity and the initial value problem (the Cauchy problem) is well–posed. Viscosity introduces implicitly a length–scale parameter into the dynamical initial–boundary value problem.

The viscoplastic regularization procedure assures the stable integration algorithm by using the finite difference method. Particular attention is focused on the well–posedness of the evolution problem (the initial–boundary value problem) as well as on its numerical solutions. The Lax–Richtmyer equivalence theorem is formulated and conditions under which this theory is valid are examined.

We take advantage of the Lax–Richtmyer equivalence theorem which says that if the evolution problem (48) is well posed for $t \in [0, t_0]$ and if it is approximated by the finite difference scheme which is consistent then the scheme is convergent to the strict solution of the evolution problem (48) if and only if it is stable.

In explicit finite element scheme for a set of the partial differential equations (48)(i) of the hyperbolic type the condition of stability is the criterion of Courant–Friedrichs–Lewy,

$$\Delta t_{n,n+1} \leq \min\left(\frac{\Delta L^n_{p,q,r}}{\left| c^n_{p,q,r} \right|} \right), \tag{51}$$

$$p = 1, 2, 3, ..., P \quad q = 1, 2, 3, ..., Q; \quad r = 1, 2, 3, ..., R,$$

where $\Delta t_{n,n+1}$ denotes time step, $c^n_{p,q,r}$ denotes the velocity of the propagation of the disturbances in the vicinity of the central node (p, q, r), $\Delta L^n_{p,q,r}$ is the minimum distance between the mesh nodes which are in the vicinity of the node.

5. IDENTIFICATION PROCEDURE

5.1. Assumption of the material functions for an adiabatic process

To do the proper identification procedure we first make assumption of the material functions (cf. Dornowski and Perzyna (2000)).

The plastic potential function f is assumed in the form (cf. Perzyna (1984) and Shima and Oyane (1976))

$$f = \left\{ J_2^{'} + \left[n_1(\vartheta) + n_2(\vartheta)\xi \right] J_1^2 \right\}^{\frac{1}{2}} \tag{52}$$

where

$$n_1(\vartheta) = 0, \qquad n_2(\vartheta) = n = \text{const.} \tag{53}$$

The isotropic work–hardening–softening function κ is postulated as (cf. Perzyna (1986a) and Nemes and Eftis (1993))

$$\kappa = \hat{\kappa}(\in^p, \vartheta, \xi) = \left\{ \kappa_s(\vartheta) - \left[\kappa_s(\vartheta) - \kappa_0(\vartheta) \right] \exp\left[-\delta(\vartheta) \in^p \right] \right\} \left[1 - \left(\frac{\xi}{\xi_F} \right)^{\beta(\vartheta)} \right], \tag{54}$$

where

$$\kappa_s(\vartheta) = \kappa_s^*(1 - \iota\overline{\vartheta}), \qquad \kappa_0(\vartheta) = \kappa_0^*(1 - \iota\overline{\vartheta}), \tag{55}$$

$$\delta(\vartheta) = \delta^*(1 - \iota\overline{\vartheta}), \qquad \beta(\vartheta) = \beta^*(1 - \iota\overline{\vartheta}), \qquad \overline{\vartheta} = \frac{\vartheta - \vartheta_0}{\vartheta_0}.$$

The overstress function $\Phi\left(\frac{f}{\kappa} - 1\right)$ is assumed in the form

$$\Phi\left(\frac{f}{\kappa} - 1 \right) = \left(\frac{f}{\kappa} - 1 \right)^m. \tag{56}$$

The evolution equation for the porosity ξ is postulated as

$$\dot{\xi} = \dot{\xi}_{grow} = \frac{g^*(\xi, \vartheta)}{T_m \kappa_0(\vartheta)} \left[I_g - \tau_{eq}(\xi, \vartheta, \in^p) \right] \tag{57}$$

where (cf. Dornowski (1999))

$$g^*(\xi, \vartheta) = c_1(\vartheta) \frac{\xi}{1 - \xi},$$

$$I_g = b_1 J_1 + b_2 \sqrt{J_2},$$

$$\tau_{eq}(\xi, \vartheta, \in^p) = c_2(\vartheta)(1-\xi)\ln\frac{1}{\xi}\left\{2\kappa_s(\vartheta) - \left[\kappa_s(\vartheta) - \kappa_0(\vartheta)\right]F(\xi_0, \xi, \vartheta)\right\}, \quad (58)$$

$$c_1(\vartheta) = \text{const}, \qquad c_2(\vartheta) = \text{const},$$

$$F(\xi_0, \xi, \vartheta) = \left(\frac{\xi_0}{1-\xi_0}\frac{1-\xi}{\xi}\right)^{\frac{2}{3}\delta} + \left(\frac{1-\xi}{1-\xi_0}\right)^{\frac{2}{3}\delta}.$$

Tabele 1. An AISI 4340 steel (plate)

$\kappa_s^* = 1155\,MPa$	$\vartheta = 293\,K$	$c_1 = 0.1$	$\xi_0 = 6\cdot 10^{-4}$	$\upsilon = 0.3$
$\kappa_0^* = 808\,MPa$	$\iota = 0.1$	$c_2 = 0.067$	$\xi_F = 0.25$	$E = 208\,GPa$
$\delta^* = 14$	$T_m = 1\,\mu s$	$b_1 = 0.58$	$n = 0.25$	$\rho_{\mathrm{Re}f} = 7850\,kg/m^3$
$\beta^* = 9$	$m = 1$	$b_2 = 1.73$	$\chi = 0.9$	$c_p = 455\,J/kgK$

As in the infinitesimal theory of elasticity we assume linear properties of the material, i.e.

$$L^e = 2\mu\mathbf{I} + \lambda(\mathbf{g}\otimes\mathbf{g}) \quad (59)$$

where μ and λ denote the Lamé constants, and the thermal expansion matrix is postulated as

$$L^{th} = (2\mu + 3\lambda)\theta\mathbf{g}, \quad (60)$$

where θ is the thermal expansion constant.

5.2. Determination of the material constants

To determine the material constants assumed we take advantage of the experimental observations presented by Chakrabarti and Spretnak (1975). They investigated the localized fracture mode for tensile steel sheet specimens simulating both plane stress and plane strain processes. The material used in their study was AISI 4340 steel. The principal variable in this flat specimen test was the width – to – thickness ratio. Variation in specimen geometry produces significant changes in stress state, directions of shear bands, and ductility. They found that fracture propagated consistently along the shear band localized region.

Let us now consider the isothermal dynamic process for a thin steel plate under condition of plane stress state. Additionally we simplify the considered adiabatic process by assumption that the evolution equation for temperature $(38)_2$ has the form

$$\dot{\vartheta} = \frac{\chi}{c_p}\tau : \mathbf{d}^p, \tag{61}$$

i.e. we postulate $\chi^{**} = 0$, $\chi^{*} = \chi$ and we neglect the nondissipative term. In fact we idealize the initial–boundary value problem investigated by Chakrabarti and Spretnak (1975) by assuming the velocity driven isothermal process for a thin steel plate. The problem has been solved by using the finite difference method.

Based on these assumptions we proceed similarly as in our previous paper, cf. Dornowski and Perzyna (2000). Then the material constants for an adiabatic process have been determined, cf. Table 1.

6. NUMERICAL EXAMPLE

6.1. Application of a finite difference method

Let us introduce in the two–dimensional Euclidean space E^2 a regular difference net of nodes (i, j) with convective coordinates $\chi^1_i = i\Delta\chi^1$ and $\chi^2_i = j\Delta\chi^2$, $i, j \in N$, where N is a set of natural numbers. Some of the nodes belong to the edge of the body and are used to approximate the boundary conditions. Time is approximated by a discrete sequence of moments $t_n = n\Delta t$, where Δt is the time step, $n \in N$.

In the convective description the metric tensor is a measure of deformation. This tensor depends on the displacement gradient. For the displacement field we postulate the following approximation in the domain $\Delta\mathrm{E}^2 = \Delta\chi^1 \times \Delta\chi^2$ of a convective difference mesh (cf. Fig. 9):

$$u_h(\chi^1, \chi^2, t) = a_1(t) + a_2(t)\chi^1 + a_3(t)\chi^2 + a_4(t)\chi^1\chi^2. \tag{62}$$

The functions $a_1(t), ..., a_4(t)$ depend only on time and are determined by the value of the function $\mathbf{u}^T_w(t) = [u_1(t), ..., u_4(t)]$ in the node points of the difference mesh (cf. Fig. 9). Hence the approximation function (56) can be written in the form:

$$u_h(\chi^1,\chi^2,t)=\mathbf{n}^T(\chi^1,\chi^2)\mathbf{u}_w(t), \tag{63}$$

where

$$\mathbf{n}=\frac{1}{4\Delta\chi^1\chi^2}\begin{bmatrix}(-\Delta\chi^1+2\chi^1)(-\Delta\chi^2+2\chi^2)\\(\Delta\chi^1+2\chi^1)(\Delta\chi^2-2\chi^2)\\(\Delta\chi^1-2\chi^1)(\Delta\chi^2+2\chi^2)\\(\Delta\chi^1+2\chi^1)(\Delta\chi^2+2\chi^2)\end{bmatrix}. \tag{64}$$

The equation (63) allows to determine values of the displacement in any point of the domain $\Delta\mathrm{E}^2=\Delta\chi^1\times\Delta\chi^2$. For the central point $\chi^1=\chi^2=0$, $n_1=\ldots=n_4=1/4$ and $n_h=(u_1+\ldots+u_4)/4$.

By using (63) we can determine the matrix of the difference operators which approximate the first partial derivatives of the displacement field,

$$\frac{\partial u_h(\chi^1,\chi^2,t)}{\partial\chi^i}=\frac{\partial\mathbf{n}^T(\chi^1,\chi^2)}{\partial\chi^i}\mathbf{u}_w(t). \tag{65}$$

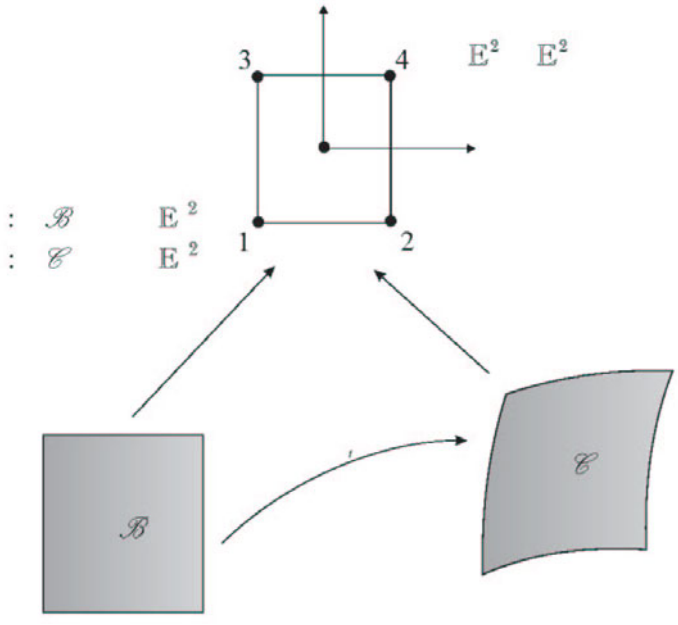

Fig. 9. Convective finite difference mesh of nodes.

6.2. Numerical solution of the initial boundary–value problem

We analyse the impact loaded plate with a pre–notched crack (Fig. 10). The material of the plate is assumed as a AISI steel and is modelled as elasto–viscoplastic with isotropic hardening–softening effects. We assume that the material softening is caused by intrinsic microdamage mechanism. The height of the specimen is equal to 200 mm, width is 100 mm and length of the initial crack (notch) is equal to 50 mm. The plane stress state is considered. As it is shown in Fig. 10, this specimen is loaded asymmetrically to the notch axis. Similar boundary value problems for the plate were analysed numerically by Li et al. (2002).

The finite difference method for regularised elasto–viscoplastic model is used[5] to obtain the solution of the formulated initial–boundary value problem. The loading condition is modelled by the velocity of nodes lying on the edge section where length equals to 50 mm, according to the relation

$$V(t) = V_0 t/t_0 \quad \text{for} \quad t \le t_0 \quad \text{and} \quad V(t) = V_0 \quad \text{for} \quad t > t_0. \tag{66}$$

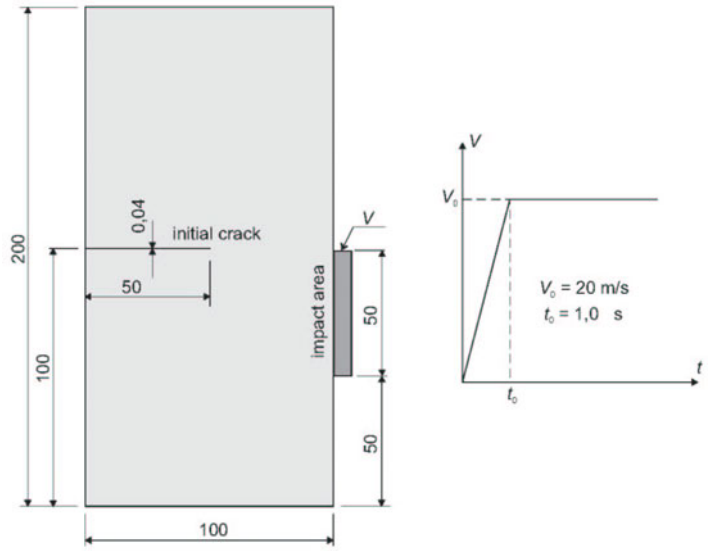

Fig. 10. The impact loaded plate with a prenotched crack.

The rise time t_0 is fixed at $1.0\,\mu$s and the speed impact $V_0 = 20$ m/s. Initial

[5]Numerical modelling of localized fracture phenomena in inelastic solids in dynamic loading processes by means of finite element method has been presented by Łodygowski and Perzyna (1997).

conditions of the problem are homogeneous. In the discussion of the numerical results attention is focused mostly on the phenomenon of crack propagation.
The finite difference method with the explicit time integration scheme (conditionally stable) is used. The stress state in a nodal environment is determined by the iterative procedure of solving the dynamical yield condition with respect to the norm of the plastic deformation rate tensor. The elaborated algorithm satisfies the material objectivity principle with respect to diffeomorphism (any motion). We assume a nonuniform mesh of nodes which contains 180 000 nodes. The smallest mesh has the dimensions $\Delta\chi^1 = \Delta\chi^2 = 40\ \mu$ m, the time increment $\Delta t = 0.00356\ \mu$ s.

Figure 11 shows distributions of normal stresses τ^{xx}, τ^{yy} and shear stress τ^{xy} at time $10\ \mu$s, a moment after the stress wave reaches the crack tip. The results illustrate the formation of the greatest stress zones, especially the shear stress in the vicinity of the notch. The characteristic unsymmetrical distribution of these zones is a result of the assumed way of loading.

In Figure 12, the evolution of the Mises stress $\tau_M = \sqrt{(2/3)\tau' : \tau'}$ in the plate is presented. The intense stress concentration is visible in the vicinity of the notch. The crack initiates from the tip of the pre–notch at $t = 47.64\ \mu$s, and grows steadily. At a certain point, it suddenly changes its direction, and grows upwards. This phenomenon can be observed more clearly in the next figure.

Figure 13 shows the Mises stress contours in the failure region following the impact. It can be clearly observed that the crack follows the path of the greatest Mises stress (the white band). The crack path changes its direction and has irregular (ragged) edges. It results from the wave character of the considered process and from the fact that the shear band transforms into an opening crack. In these pictures the used mesh of nodes is also shown.

In Figure 14 the equivalent plastic strain distribution is displayed. It shows that there is a strain concentration region right in the front of the pre–notch tip. Along with the shear band progress the equivalent plastic strain intensity decreases. That confirms the fact, that the shear band transforms into an opening crack.

The evolution of temperature is shown in Fig. 15. Zones of increased temperature correspond to the plastic zones. The maximum value of temperature is $\vartheta_{max} = 750$ K. The effect of such a strong heating of the material results from its mechanical properties, i.e. the high strength steel, $R_m = 2000$ MPa. >From Fig. 15 one may see that the computed temperature distribution is very heterogeneous. A similar effect has been noticed in experimental observations by Guduru et al. (2001).
In Figure 16 the evolution of microdamage is presented. It can be clearly ob-

served that the crack path (a black line) is very irregular and it widens steadily.

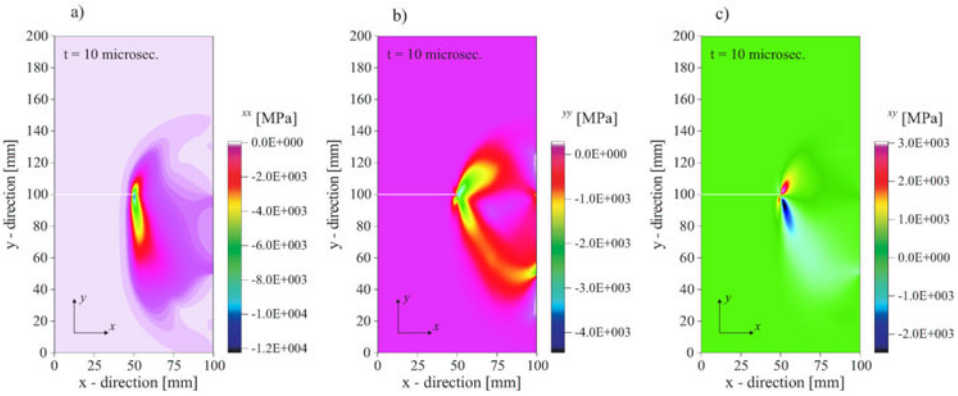

Fig. 11. The contour of normal stresses τ^{xx}, τ^{yy} (a, b), and (c) shear stress τ^{xy} in the plate at $t = 10\ \mu$ s.

A dependence on time for various process variables at the initial crack tip is plotted in Figs 17 and 18. A dependence of the Mises stress on the equivalent plastic deformation at the considered node is presented in Fig. 18. Figure 18 illustrates mainly the nonelastic stress–strain characteristic of the plate material. At the beginning of the deformation process the material undergoes isotropic hardening, and next after certain time period the material softening takes place. The evolutional softening effects are very well visible here.

6.3. Discussion of the numerical results

From the results presented in Fig. 14 we see that the localized fracture is preceded by the propagation of shear band[6]. This is also very visible in Fig. 16, where the propagated localized region of critical microdamage (it means the fracture front for $\xi = \xi^F$) is preceded by the shear band region along which the microdamage is smaller than $\xi = \xi^F$. Very important result may be observed in Fig. 15, where the evolution of temperature is obtained as nonuniform. This result is in agreement with the experimental observations presented by Guduru, Rosakis and Ravichandran (2001). They observed (cf. Fig. 7) that the temperature distribution along the shear band is highly nonuniform, with discrete region of high temperature, that looks like "hot spots". We suggest that the reason of this phenomenon is caused by interaction of dispersive stress waves during observed adiabatic process.

[6] For a thorough discussion of numerical investigation of propagation of shear bands in inelastic solids please consult Glema, Łodygowski and Perzyna (2004).

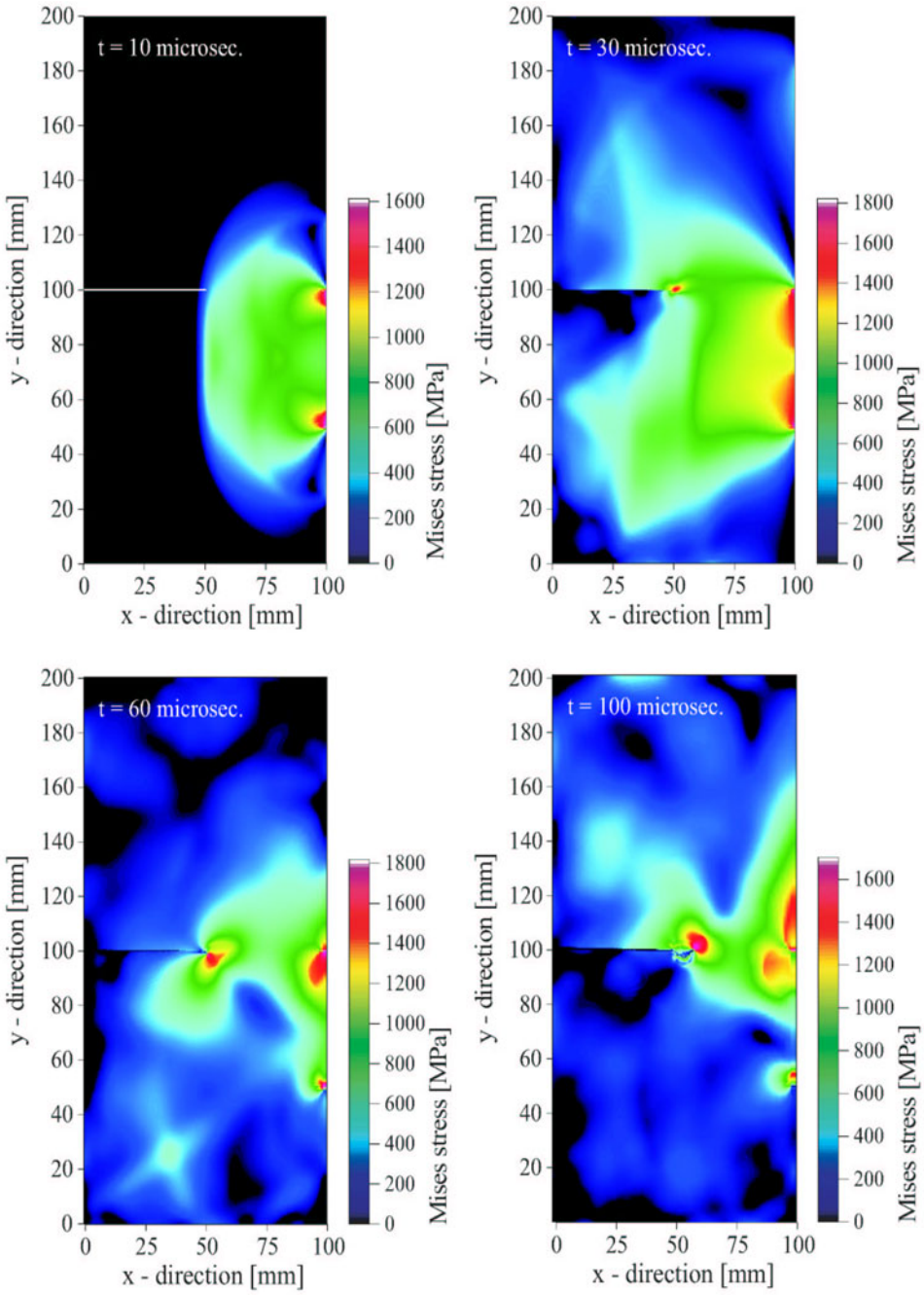

Fig. 12. Evolution of the Mises stress in the plate.

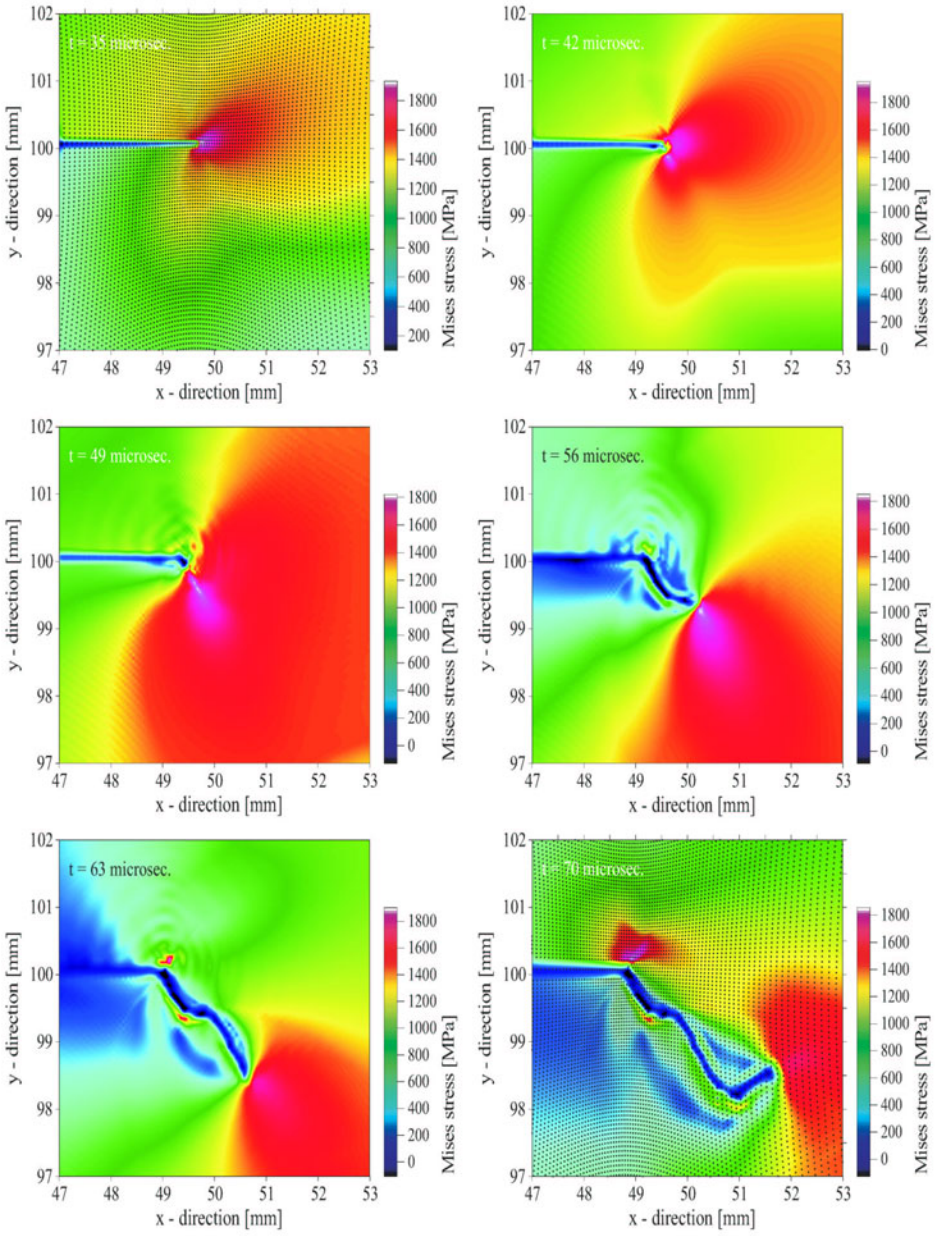

Fig. 13. Mises stress contours in the failure region.

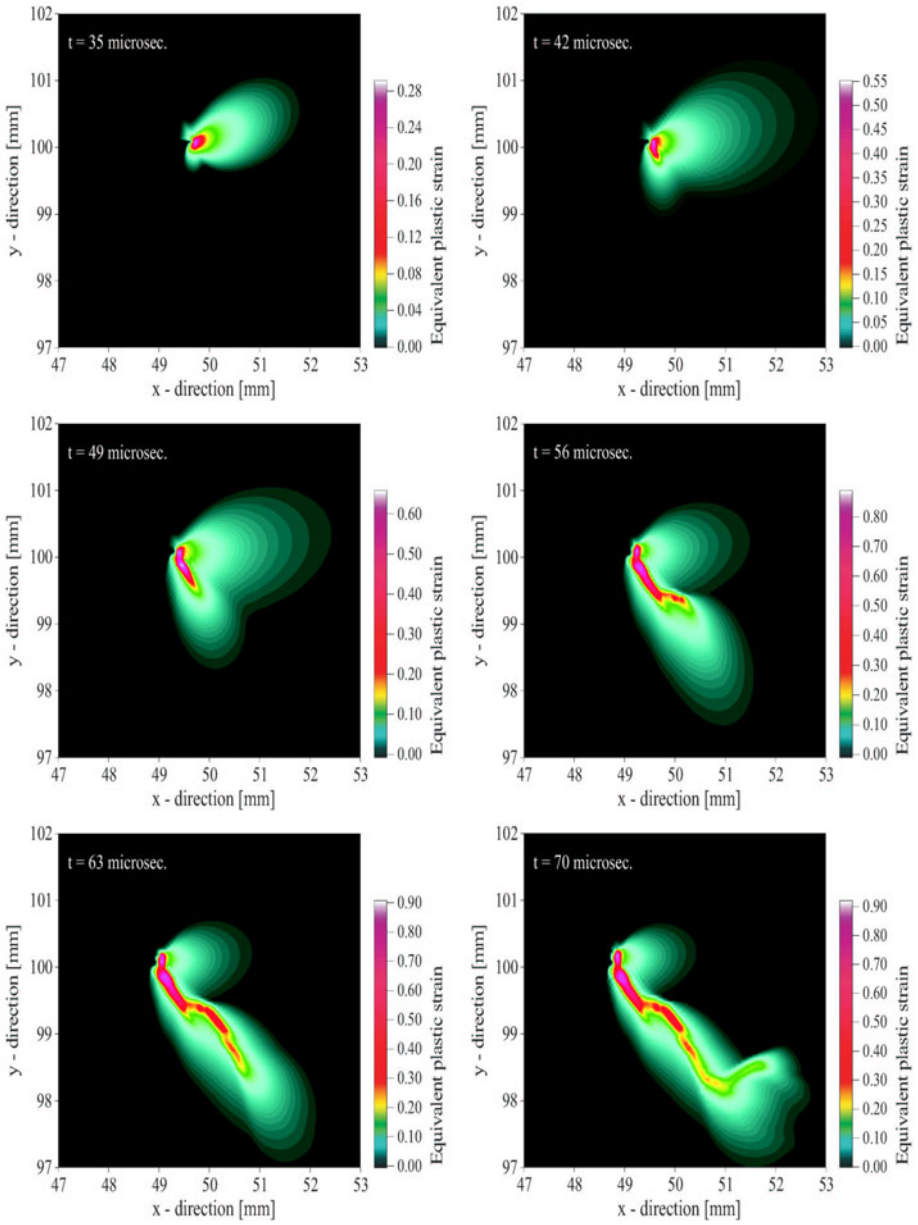

Fig. 14. Evolution of the equivalent plastic deformation in the fracture region.

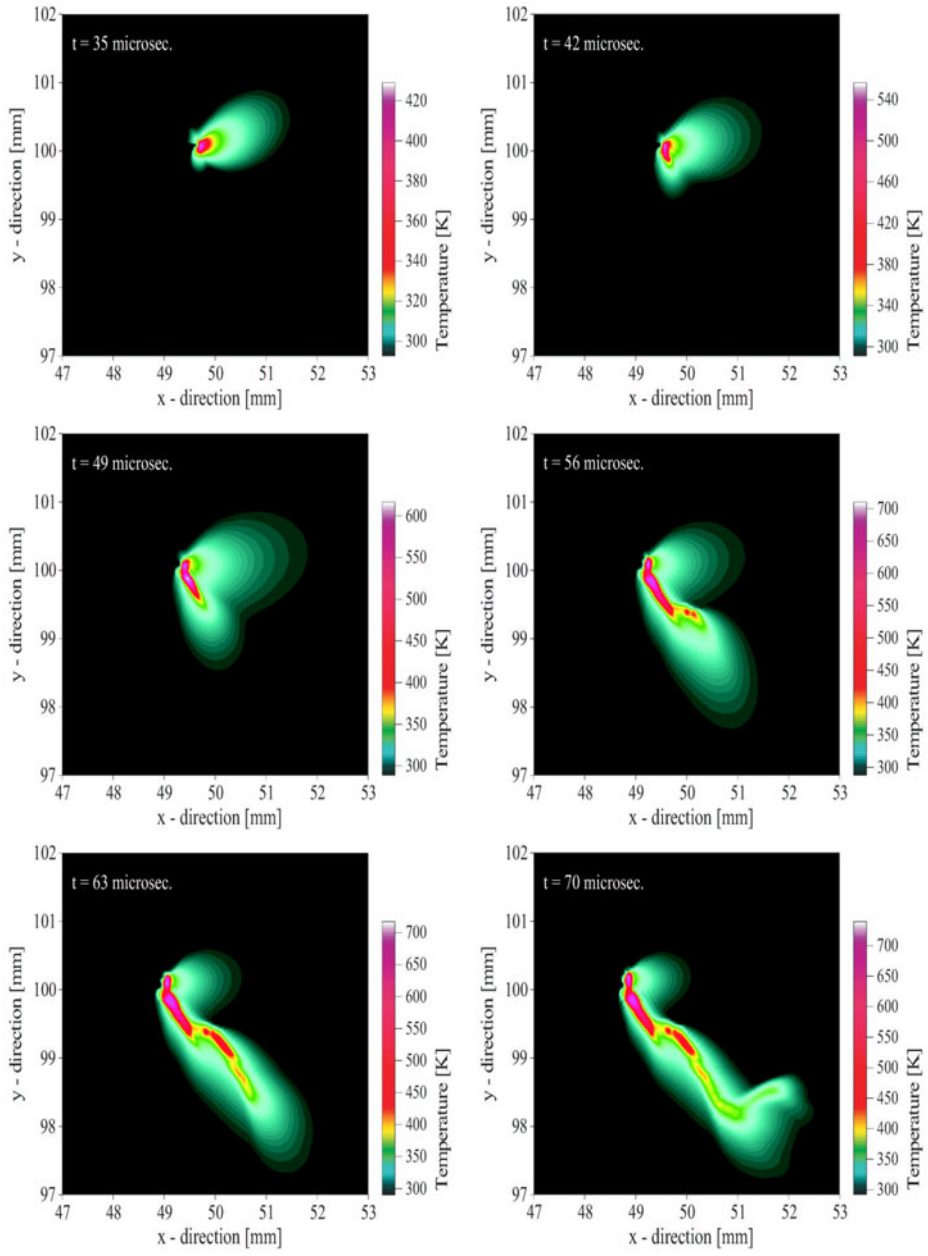

Fig. 15. Evolution of temperature in the fracture region.

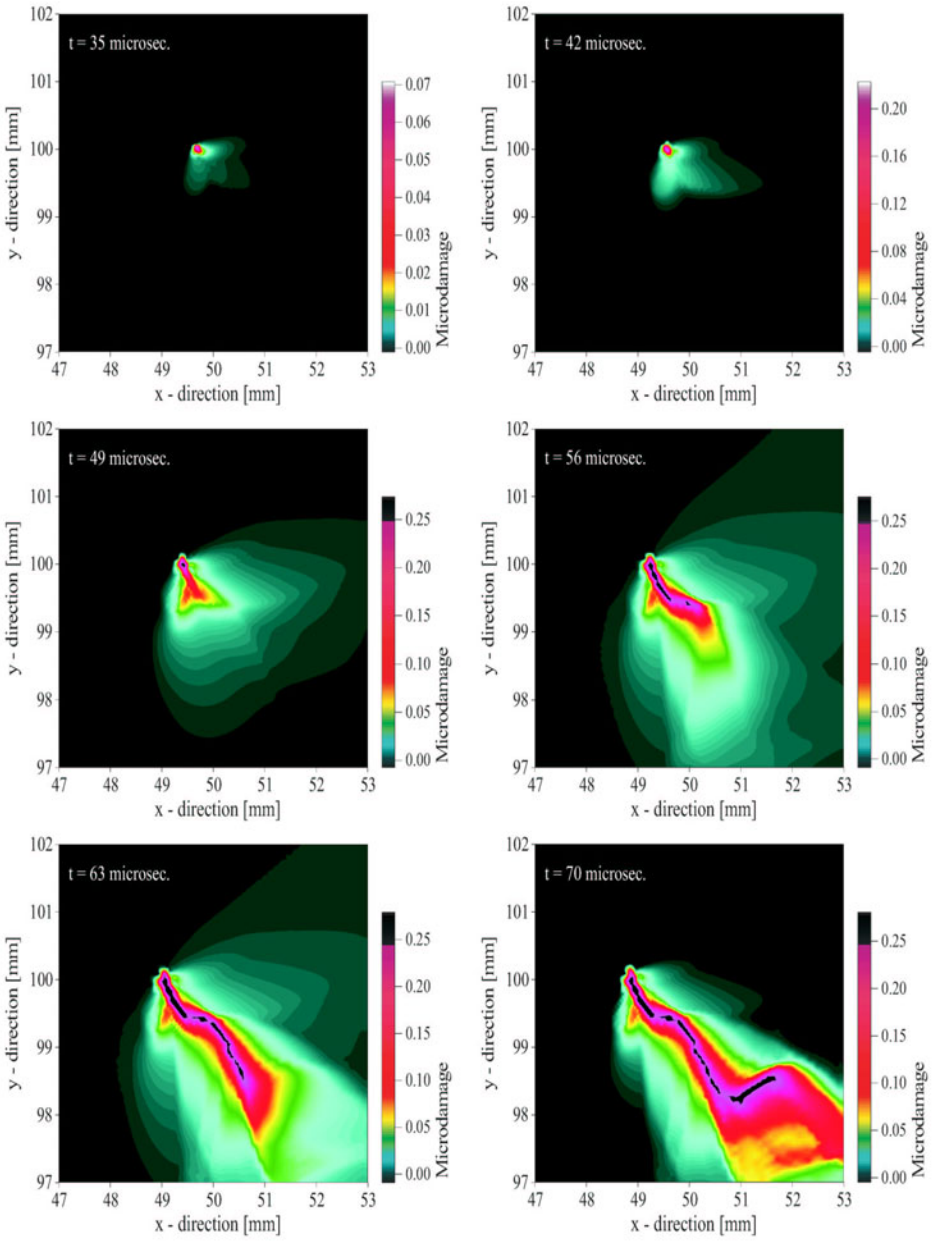

Fig. 16. Evolution of the microdamage and the crack path in the fracture region.

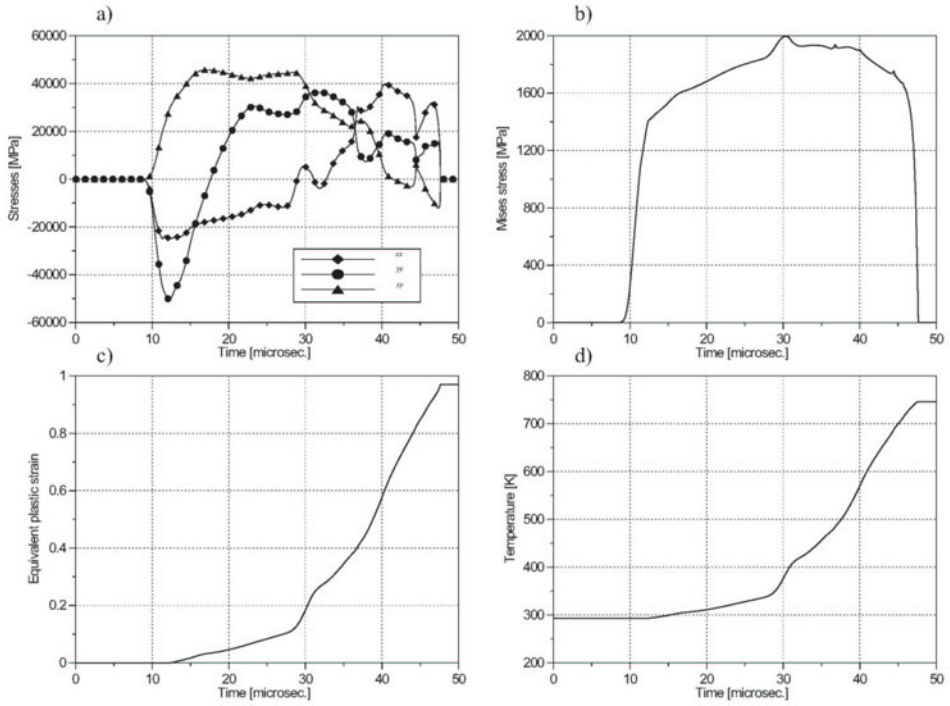

Fig. 17. (a) Stress components, (b) Mises stress, (c) equivalent plastic strain and (d) temperature at the initial crack tip as a function of time.

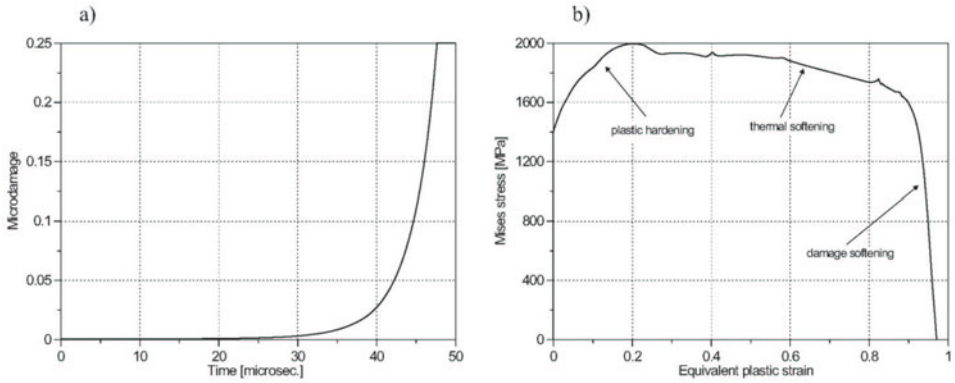

Fig. 18. (a) Microdamage at the initial crack tip as a function of time, (b) Mises stress at the initial crack tip as a function of the equivalent plastic strain.

The evolution of the microdamage and the crack path in the fracture region shown in Fig. 16 indicates that the crack path is very irregular and it widens steadily. It seems that in some places of the crack we can expect the branching effect as it has been observed by Guduru, Rosakis and Ravichandran (2001), Of

course, we have to take into account that they investigated real material (C 300 steel) which has some impurities, while we assumed fully homogeneous material of the plate for our numerical simulations.

We can conclude that the shear band branching can be generated by interaction of dispersive stress waves during adiabatic process and by some existing impurities of the investigated material.

7. EPILOGUE

The elaborated numerical algorithm satisfies the material objectivity principle with respect to diffeomorphism (any motion). The discretisation parameters are assumed in such a way that the problem of mesomechanics is solved properly. A thin shear band region of finite width which undergoes significant deformation and temperature rise has been determined. Its evolution up to the occurrence of final fracture has been simulated. Shear band advance, as the function of time and the evolution of the Mises stress, equivalent plastic deformation, temperature and the crack path in the fracture region has been determined. Qualitative comparison of numerical results with experimental observation data has been presented. Based on this comparison we can conclude that our numerical results are in accord with the experimental observations performed by Guduru, Rosakis and Ravichandran (2001). Particularly, in our numerical simulation the temperature evolution along the shear band region is very nonuniform and the obtained crack path is very irregular and is showing a tendency to the branching phenomenon similarly as have been suggested by experimental observations. The obtained numerical results have

proven the usefulness of the thermo–elasto–viscoplastic theory in the numerical investigation of dynamic shear band propagation.

REFERENCES

1. Abraham, R., Marsden, J.E., and Ratiu, T. (1988) *Manifolds, Tensor Analysis and Applications.* Springer, Berlin.
2. Chakrabarti, A.K., and Spretnak, J.W. (1975) "Instability of plastic flow in the direction of pure shear." *Metallurgical Transactions*, **6A**, 733–747.
3. Chi, Y.C., Lee, S.H., Cho, K. and Duffy, J. (1988) *The effects of tempering and test temperatures on the dynamic fracture initiation behaviour of an AISI 4340 VAR steel*. Brown University Technical Report, August.
4. Cho, K., Chi, Y.C. and Duffy, J. (1988) *Microscopic observations of adiabatic shear bands in three different steels*. Brown University Report No DAAL03-88-K-0015/3, September.

5. Coleman, B.D., and Noll, W. (1963) "The thermodynamics of elastic materials with heat conduction and viscosity." *Arch. Rational Mech. Anal.*, **13**, 167–178.
6. Curran, D.R., Seaman, L., and Shockey, D.A. (1987) "Dynamic failure of solids." *Physics Reports*, **147**, 253–388.
7. Dornowski, W. (1999) "Influence of finite deformation on the growth mechanism of microvoids contained in structural metals." *Arch. Mechanics*, **51**, 71–86.
8. Dornowski, W., and Perzyna, P. (1999) "Constitutive modelling of inelastic solids for plastic flow processes under cyclic dynamic loadings." *Transaction of the ASME, J. Eng. Materials and Technology*, 121, 210–220.
9. Dornowski, W., and Perzyna, P. (2000) "Localization phenomena in thermo–viscoplastic flow processes under cyclic dynamic loadings." *CAMES*, **7**, 117–160.
10. Dornowski, W. and Perzyna, P. (2002) "Numerical analysis of macrocrack propagation along a bimaterial interface under dynamic loading processes". *Int. J. Solids and Structures*, **39**, 4949–4977.
11. Duszek, M.K. and Perzyna, P. (1991) "The localization of plastic deformation in thermoplastic solids". *Int. J. Solids Structures*, 27, 1419–1443.
12. Duszek–Perzyna, M.K. and Perzyna, P. (1994) "Analysis of the influence of different effects on criteria for adiabatic shear band localization in inelastic solids". In Proceedings *Material Instabilities: Theory and Applications*, ASME Congress, Chicago, 9–11 November 1994 (Eds. R.C. Batra and H.M. Zbib), AMD–Vol. **183**/MD–Vol. **50**, ASME, New York, pp. 59–85.
13. Glema, A., Łodygowski, T. and Perzyna, P. (2004) "Numerical investigation of dynamic shear bands in inelastic solids as a problem of mesomechanics" International Congress of Theoretical and Applied Mechanics, 15–21 August, 2004, Warsaw, Poland.
14. Guduru, P.R., Rosakis, A.J. and Ravichandran, G. (2001) "Dynamic shear bands: an investigation using high speed optical and infrared diagnostic". *Mechanics of Materials*, **33**, 371–402.
15. Hutchinson, J.W. (2000) "Plasticity at the micron scale". *Int. J. Solids and Structures*, **37**, 225–238.
16. Johnson, J.N. (1981) "Dynamic fracture and spallation in ductile solids." *J. Appl. Phys.*, **52**, 2812–2825.
17. Li, S., Liu, W.–K., Qian, D., Guduru, P.R. and Rosakis, A.J. (2001) "Dynamic shear band propagation and micro–structure of adiabatic shear band". *Comput. Methods Appl. Mech. Engng.*, **191**, 73–92.
18. Łodygowski, T. and Perzyna, P. (1997) "Numerical modelling of localized fracture of inelastic solids in dynamic loading processes". *Int. J. Num. Meth. Engng.*, **40**, 4137–4158.
19. Marsden, J.E., and Hughes, T.J.R. (1983) *Mathematical Foundations of*

Elasticity. Prentice–Hall, Englewood Cliffs, New York.
20. Needleman, A. (2000) "Computational mechanics at the mesoscale". *Acta Materialia*, **48**, 105–124.
21. Nemes, J.A., and Eftis, J. (1993) "Constitutive modelling of the dynamic fracture of smooth tensile bars." *Int. J. Plasticity*, **9**, 243–270.
22. Oldroyd, J. (1950) "On the formulation of rheological equations of state." *Proc. Roy. Soc. (London)* **A 200**, 523–541.
23. Perzyna, P. (1963) "The constitutive equations for rate sensitive plastic materials". *Quart. Appl. Math.*, **20**, 321–332.
24. Perzyna, P. (1966) "Fundamental problems in viscoplasticity". *Advances in Applied Mechanics*, **9**, 243–377.
25. Perzyna, P., 1971. "Thermodynamic theory of viscoplasticity". *Advances in Applied Mechanics*, **11**, 313–354.
26. Perzyna P. (1984) "Constitutive modelling of dissipative solids for postcritical behaviour and fracture". *ASME J. Eng. Materials and Technology*, **106**, 410-419.
27. Perzyna, P. (1986a) "Internal state variable description of dynamic fracture of ductile solids". *Int. J. Solids Structures*, **22**, 797-818.
28. Perzyna, P. (1986b) "Constitutive modelling for brittle dynamic fracture in dissipative solids". *Arch. Mechanics*, **38**, 725–738.
29. Perzyna, P. (1995) "Interactions of elastic–viscoplastic waves and localization phenomena in solids". In Proceedings *IUTAM Symposium on Nonlinear Waves in Solids*, August 15–20, 1993, Victoria, Canada; (Eds. J.L. Wegner and F.R. Norwood), ASME 1995, pp. 114–121.
30. Perzyna, P. (2001) "Thermo–elasto–viscoplasticity and damage". In *Handbook of Materials Behaviour Models*. (Ed. J. Lemaitre), Academic Press, New York, pp. 821–834.
31. Perzyna, P. (2005) "The thermodynamical theory of elasto–viscoplasticity". *Engineering Transations*, **53**, 235-316.
32. Perzyna, P., and Drabik, A. (1989) "Description of micro–damage process by porosity parameter for nonlinear viscoplasticity". *Arch. Mechanics*, **41**, 895–908.
33. Perzyna, P., and Drabik, A. (2006) "Micro–damage mechanism in adiabatic processes". *Engineering Transations* (submitted for publication).
34. Shima, S., and Oyane, M. (1976) "Plasticity for porous solids." *Int. J. Mech. Sci.*, **18**, 285–291.
35. Shockey, D.A., Seaman, L., and Curran, D.R. (1985) "The microstatistical fracture mechanics approach to dynamic fracture problem." *Int. J. Fracture*, **27**, 145–157.
36. Sidey, D., and Coffin, L.F. (1979) "Low–cycle fatigue damage mechanism at high temperature." In *Fatigue Mechanism, Proc. ASTM STP 675 Symposium* Kansas City, Mo., May 1978, (J.T. Fong, Ed.), Baltimore, pp. 528–568.

37. Sluys, L.J. (1992) *Wave propagation, localization and dispersion in softening solids.* Doctoral thesis, Delft Uniwersity Press, Delft.
38. Truesdell C., and Noll W. (1965) *The nonlinear field theories.* Handbuch der Physik, Band III/3, pp. 1–579, Springer, Berlin.
39. Zhou, M., Rosakis, A.J. and Ravichandran G. (1996) "Dynamic propagating shear band in impact–loaded prenotched plates. I. Experimental investigations of temperature signatures and propagation speed". *J. Mech. Phys. Solids*, **44**, 981–1006.
40. Zhou, M., Ravichandran G. and Rosakis, A.J. (1996) "Dynamic propagating shear band in impact–loaded prenotched plates. II. Numerical simulations". *J. Mech. Phys. Solids*, **44**, 1007–1032.

The paper is dedicated to Professor Andrzej Garstecki on the occasion of His 70^{th} birthday.